Assimilation of Visible-Band Satellite Data for Mesoscale Forecasting in Cloudy Conditions

ALAN E. LIPTON* AND GEORGE D. MODICA*

Optical Effects Division, Geophysics Directorate, Air Force Research Laboratory, Hanscom Air Force Base, Massachusetts

(Manuscript received 3 October 1997, in final form 13 April 1998)

ABSTRACT

Assimilation of satellite data can enhance the ability of a mesoscale modeling system to produce accurate short-term forecasts of clouds and precipitation, but only if there is a mechanism for the satellite-derived information to propagate coherently from the analysis into the forecast period. In situations where stratiform cloud cover inhibits surface heating, assimilation of visible image data can be beneficial for analyses, but those data present particular challenges for application to numerical forecasts. To address the forecast problem, a method to adjust the humidity field and the radiative parameterization of a model was developed such that satellite retrievals of cloud properties have an impact that extends well into the forecast. The adjustment directs the model's cloud diagnosis and radiation algorithms to produce results that agree with satellite retrievals valid at the forecast initiation time. Experiments showed a high level of fidelity between a short-term forecast made with this method and coincident analyses produced with satellite data. In comparison with a forecast made using a standard model formulation, the adjusted model produced 1) surface insolation fields that were far more realistic, 2) more accurate shelter-height temperatures, and 3) mesoscale circulation features that were more consistent with observed diurnal convective cloud development.

1. Introduction

Clouds and their effect on the surface energy budget are deservedly the topic of much discussion and research in numerical weather prediction. One common motivation for addressing this subject is a desire to improve a prediction model's capability to simulate the evolution of important mesoscale patterns. The U.S. Air Force (USAF) is among those with an interest in improving this capability, particularly with regard to short-term forecasts of clouds and precipitation over small ($\sim$500 $\times$ 500 km^2) regions.

Lipton (1993) addressed this issue through time-continuous assimilation of cloud radiative characteristics retrieved from geostationary satellite data. That study demonstrated that the inclusion of satellite-retrieved cloud characteristics had beneficial effects on the analysis, but the study did not deal with the forecasting problem. The assimilation method ensured that the impact of clouds on the surface energy budget was appropriately represented during the analysis, but provided no mechanism for the cloud radiative forcing to be maintained during a forecast. In the forecast period, the model could only revert to its standard radiation procedure. Without continued satellite-derived forcing, there is a tendency for a mesoscale model solution to lose any information that had been provided during assimilation, due to the influence of the boundary conditions (Vukicevic and Paegle 1989).

This forecast problem has led researchers to seek ways to improve models' capability to depict cloud and radiation features that are detected in satellite data. One such method, developed by Wu and Smith (1992), involves tuning the algorithm the model uses to diagnose cloudiness as a function of relative humidity. They devised a method to alter the function, such that model-computed values of outgoing longwave radiation would agree more closely with satellite-retrieved values. Their approach can bring about modest changes to the modeled cloud fields, but it can provide little benefit in situations where there are large discrepancies between the model relative humidity fields and the satellite-observed cloud fields, as is often the case in mesoscale modeling. In such cases, achieving a match between the model and the satellite data without radically changing the model formulation would require altering the model relative humidity fields, so that the areas with high humidity would occur where the satellite showed clouds to be present.

* Current affiliation: Atmospheric and Environmental Research, Inc., Cambridge, Massachusetts.

Corresponding author address: Dr. Alan E. Lipton, Atmospheric and Environmental Research, Inc., 840 Memorial Dr., Cambridge, MA 02139-3794.
E-mail: alipton@aer.com

Several researchers have used satellite image data, along with other data, to alter a numerical analysis of humidity. The idea is that the satellite data can be used to infer cloudiness, and the humidity must be at or near saturation within the clouds. Wolcott and Warner (1981) used infrared satellite images to estimate cloud-top altitude and assumed the thickness of nonprecipitating clouds to be one model grid level. Albers et al. (1996) and Macpherson et al. (1996) described systems that generate three-dimensional cloud analyses using a variety of data, including satellite imagery, surface observations, and radar data. The cloud analyses provide input to mesoscale humidity analyses. Koch et al. (1997) used a satellite-based cloud classification scheme and specified model humidity profiles according to the classifications. This later method relied heavily on radiosonde data.

For the study reported here, we developed a method that relies primarily on satellite data to estimate the positions and extents of cloud layers. The model relative humidity is then altered, such that the model's cloud diagnosis algorithm yields results that agree with the satellite retrievals at the satellite analysis time. In addition, the model parameterization that deals with the transmission of solar radiation through clouds is tuned to match observed conditions at the forecast initiation time. The object of the tuning is to obtain as much agreement as possible between the surface insolation computed with the parameterization and the insolation inferred with the aid of visible satellite data. Experimental forecasts were made with the tuned parameterization, using the altered relative humidity fields as initial conditions.

2. Assimilation objective

The method we developed for preparing the model and its data fields for a cloud forecast is directly tied to the Lipton (1993) method of four-dimensional analysis. Together, the methods are designed to improve the model's representation of cloud radiative effects throughout the analysis and forecast periods. The methods are described here with reference to a case in which shading of the ground by a field of stratiform clouds had a pronounced influence on the mesoscale meteorology.

a. Use of satellite data to drive modeled insolation

The assimilation of satellite data for this case was performed with the National Center for Atmospheric Research–Pennsylvania State University (NCAR–PSU) Mesoscale Model 4 (MM4) version 8, which is a different model than the one used in the Lipton (1993) study. The primary relevant features of the MM4 are listed in Table 1. The area covered by the nested grid, exclusive of its outer four rows and columns, is referred to as the domain for this case and is the area covered by the model output plots that follow.

TABLE 1. Features of the NCAR–PSU mesoscale model.

Horizontal grid	Arakawa B grid; 50 × 55, 45 km (outer grid) and 67 × 85, 15 km (nested grid)
Vertical grid	Staggered; variable resolution, σ coordinate; 28 levels
Boundary layer	High resolution; *K* theory with nonlocal plume model for unstable regime (Zhang and Anthes 1982)
Cumulus convection	Modified Kuo (Anthes 1977)
Initial condition	Standard surface and rawinsonde data from 0700 EST (1200 UTC) 23 Aug 1993; successive-corrections objective analysis with NCEP global analysis as first guess (Benjamin and Seaman 1985); implicit normal mode initialization (Errico and Bates 1988)

The MM4 holds ocean surface temperatures constant, using values from the National Centers for Environmental Prediction (NCEP) global analysis. In land areas, the MM4 computes surface temperatures using a prognostic surface energy budget equation that includes terms representing sensible and latent heat fluxes to the atmosphere, sensible heat fluxes into the soil, and solar and infrared radiative fluxes (Zhang and Anthes 1982). The standard MM4 formulation, without satellite data assimilation, computes the surface insolation under cloudy conditions ($Q^M_{s\,(\text{cloudy})}$) on the basis of fractional cloud cover parameters n_i that are computed from the relative humidity field. The subscript, *i*, refers to the layers of cloud represented in the model.

With satellite data assimilation (Lipton 1993), a person–computer interactive program is used to discriminate cloudy and clear areas of visible and infrared satellite images from the Geostationary Operational Environmental Satellite (GOES) Visible and Infrared Spin Scan Radiometer (VISSR). Within the cloudy areas, a simple radiative transfer model is used to retrieve the cloud reflectance and the cloud effective solar transmittance (τ_{eff}) from visible image data. An inverted parameterization infers vertically integrated cloud liquid water (*W*) from cloud reflectance. The integrated liquid water, in turn, is input to another parameterization to make an estimate of the cloud infrared emittance. The retrieved values of τ_{eff} and the cloud infrared emittance are averaged from satellite pixels to the model grid resolution and then assimilated into the model. The model handles temporal interpolation from satellite observation times to model time steps. When this assimilation method is applied to the MM4, the the surface insolation is computed from

$$Q_{s\,(\text{cloudy})} = Q_{s\,(\text{clear})}\tau_{\text{eff}}, \quad (1)$$

where $Q_{s\,(\mathrm{clear})}$ is the insolation computed by the model's ordinary radiation parameterization for clear skies.

b. Demonstration case

The case for which the assimilation and forecast experiments were performed was 23 August 1993. On that day, the weather pattern over the southeastern United States exhibited weak synoptic-scale dynamics. At the surface, there were no strong frontal boundaries. A sea level pressure ridge extended into North Carolina from the northeast, with weak northeasterly flow to the south. The surface wind flow was light and westerly over Mississippi and Alabama, and during the course of the morning, southwesterly flow developed over Tennessee and Kentucky in advance of an approaching surface cold front. The surface weather was predominantly hot and humid, with shelter-height temperatures reaching maxima of about 35°C (95°F) over much of the area, and with dewpoint temperatures around 24°C (75°F) in some places.

In the morning, stratiform clouds covered a broad region from central Georgia to western North Carolina (Fig 1a). Most of the stratiform region was free of precipitation, although an embedded convective cloud produced a modest amount of rain in southern North Carolina (3 mm at Charlotte) and brief, light showers occurred in western South Carolina and northern Georgia. The stratiform clouds dissipated slowly during the morning so that, by early afternoon (Fig. 1b), the dissipation was nearly complete. During the morning, convective clouds developed in most of the area surrounding the dissipating stratiform cloud deck. This development indicates that strong ground warming and convective destabilization were prevalent, except where they were locally inhibited by shading in the areas covered by stratiform clouds. Shelter-height temperatures in the shaded areas increased by <6°C during the 6-h period from 0700 to 1300 EST, while increases of $\sim$10°C were typical in the surrounding areas. Convective development was strong to the northwest of the stratiform cloud area, in the mountainous areas of western North Carolina, but it never achieved great intensity there. Development was strongest in southeast Georgia and in eastern Alabama (Fig. 1c), where deep convection persisted into the early evening. Convective clouds were present also along a sea-breeze convergence zone inland from the coastlines of Georgia and the Carolinas (Fig. 1c).

The assimilation data used in this study were from *GOES-7,* which had the ability to take image data in one visible band and in several infrared bands. The visible data were taken at a nominal ground resolution of 1 km. Seven image datasets, taken hourly over the period 0700–1300 EST 23 August 1993, were obtained from the archives of the University of Wisconsin Space Science and Engineering Center. It was necessary to calibrate the visible-band data because, for *GOES-7* and previous GOES satellites, the visible channel data were not automatically calibrated. A model-relative calibration method was used (Lipton 1993), referenced to pyranometer data from a station in the Historically Black Colleges and Universities Solar Measurement Network (see http://rredc.nrel.gov/solar/old_data/hbcu for more information).

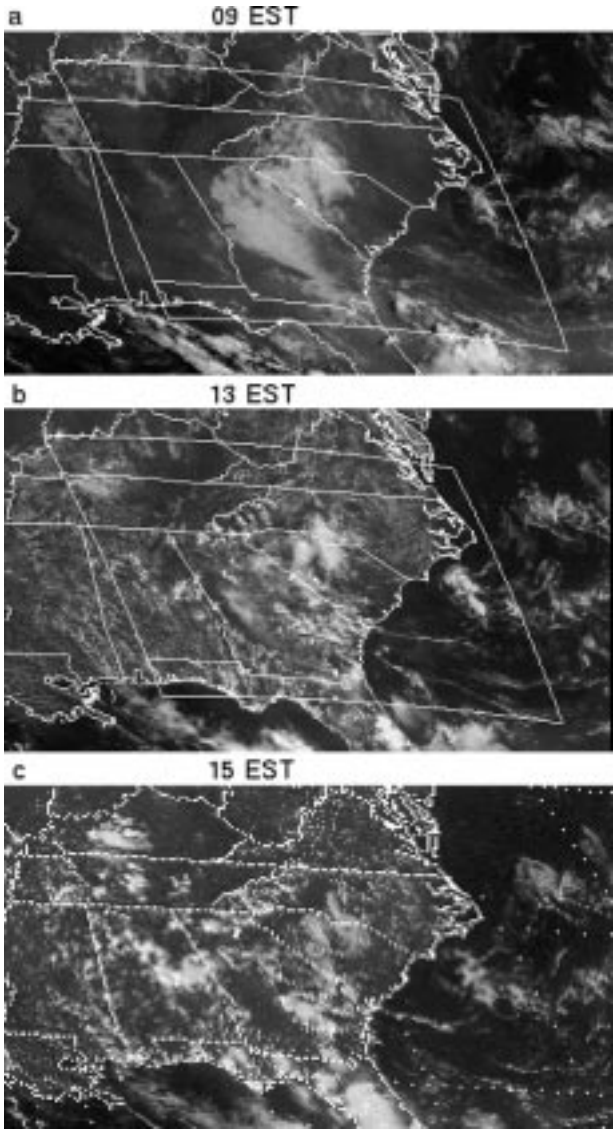

FIG. 1. GOES visible satellite images at (a) 0900, (b) 1300, and (c) 1500 EST 23 Aug 1993. The analysis domain is outlined in (a) and (b). Panel (c) was generated from a different data archive than (a) and (b), with a coarser image resolution.

The assimilation experiments were initiated at 0700 EST (1200 UTC) 23 August 1993 using the conventional NCEP global analysis, reanalyzed with standard National Weather Service rawinsonde and surface data. Satellite retrievals were used to drive the model's insolation values, as described above, for the period 0700–1000 EST, using hourly satellite image data. At the 1000

EST point, the model humidity fields were altered and the solar radiation parameterization was tuned, as described below, and a 9-h forecast was initiated.

3. Humidity adjustment method

a. Overview of method

There are several major steps in the method we used to specify adjustments to the model humidity. First, infrared satellite data are used to retrieve the altitudes of the cloud tops. Then cloud geometric thicknesses are estimated using retrievals of vertically integrated cloud liquid, derived from visible-channel satellite data. Cloud-base altitudes are computed by combining the cloud-top and -thickness data. The cloud-top and -base data from the satellite retrievals are used to compute the fractional cloud cover at each grid level within each model grid box. The model relative humidity at each grid point is then altered to cause agreement between the model-computed and satellite-derived cloud fractions. These steps are described in the remainder of this section.

b. Cloud-top retrieval

The method for retrieving cloud-top altitudes depends on the relationship between the cloud's altitude and its temperature. The method relies on data from the VISSR longwave window channel at 11 μm, where images are composed of pixels with dimensions of about 8 km at nadir.

The infrared radiance (L) for the 11-μm channel, in a partly cloudy field of view, can be expressed as

$$L = f\varepsilon_c L_{\text{cloud}} + (1 - f\varepsilon_c)L_{\text{clear}}, \quad (2)$$

where f is the fractional cloud cover in the field of view, ε_c is the cloud emittance, and the remaining terms are the radiances that would occur if the field of view were clear (L_{clear}) or covered by opaque clouds (L_{cloud}). It is assumed that each field of view has a clear part and a cloudy part, each of which is horizontally uniform. The clear and cloud radiances can be computed by

$$L_{\text{clear}} = \varepsilon_s B(T_s)\tau(p_s) + \int_{\tau(p_s)}^{1} B[T(p)]\, d\tau(p) \quad (3)$$

and

$$L_{\text{cloud}} = B[T(p_c)]\tau(p_c) + \int_{\tau(p_c)}^{1} B[T(p)]\, d\tau(p), \quad (4)$$

where the subscripts s and c refer to conditions at the surface and the cloud top, respectively; T is the temperature; p is the pressure; B is the Planck (blackbody) radiance; and $\tau(p)$ is the transmittance from pressure level p to space. The variables in these equations are not strictly monochromatic, but are representative of the spectral response of the imager.

For these retrievals, the values of L_{clear} were computed at each field of view using the radiative transfer method employed by Smith (1983). Data for the computations were taken from the nearest grid point of the numerical model. The model surface (skin) temperature was used, and the model profiles of temperature and water vapor were vertically interpolated to the standard levels employed in the radiative transfer computations. For levels above the top of the model, climatological data were used.

The values of ε_c and f used in (2) were derived from the cloud parameter retrievals valid at 1000 EST. The cloud emittance retrievals generated from 1-km-resolution visible image data were averaged over all cloudy pixels within each 8-km infrared pixel to obtain ε_c. The computations of f were based on the cloud–clear discrimination product that had been prepared at 1-km resolution. The number of cloud-flagged pixels was divided by the total number of 1-km pixels within each infrared pixel ($8 \times 8 = 64$) to arrive at the value of f.

With a measured value of L and computed values of L_{clear}, ε_c, and f, it was possible to solve (2) for L_{cloud}:

$$L_{\text{cloud}} = L_{\text{clear}} + \frac{L - L_{\text{clear}}}{f\varepsilon_c}. \quad (5)$$

The value of L_{cloud} can also be computed from (4), given temperature and water vapor data from the mesoscale model and an estimate of the pressure at the cloud top. The cloud-top pressure was retrieved by first taking the cloud-top pressure to be the same as the surface pressure and then reexecuting (4) with successively lower values of the cloud-top pressure until the value of L_{cloud} agreed with the result from (5). The cloud-top pressure was limited to a minimum of 115 hPa and a maximum of $(p_s - 50)$ hPa.

We added two additional features to the cloud-top retrieval procedure to cope with situations that might lead to erroneous retrievals. In one such instance, the surface temperatures from the model were adjusted downward by 2°C before they were used in the radiative transfer computations. The adjustments were made because the computed radiances for clear areas were found to be biased in relation to the observed radiances. The adjustment was roughly consistent with a bias that had been found between modeled (with satellite assimilation) and observed shelter-height temperatures. In addition, features were added to account for the high sensitivity of the result of (5) to errors in $L - L_{\text{clear}}$ when f is small. Infrared pixels with $f \leq 0.05$ were treated as cloud free. For pixels with $0.05 < f \leq 0.30$, the retrieved p_c was replaced by the value from whichever neighboring pixel had the largest value of f. Neighboring is defined here as within two rows or columns from the pixel.

c. Cloud-base retrieval

The cloud-base pressure retrievals relied on estimating the distance between cloud top and base, making

an assumption about the vertical distribution of cloud liquid water between those levels. The estimate of the total cloud liquid water content was taken from the retrievals generated from the 1000 EST visible imagery. The vertical distribution of that water was assumed to be proportional to what would be produced by pseudoadiabatic ascent from cloud base to cloud top. We thus assumed that there was only one cloud layer. The details of the method are given below.

The method uses temperature profile data from the MM4 horizontal grid point nearest to the visible image-pixel being considered. A saturated parcel of air is assumed to exist at the temperature and pressure of the first MM4 level below the cloud top. We compute the total condensed liquid water (W_a) that would be produced during pseudoadiabatic ascent from that level to the level of the cloud top. The computed value W_a is compared with the retrieved value of total cloud liquid water, W. If $bW_a < W$, where b is defined below, then the process is repeated for the next lower MM4 level, and so on until the inequality no longer holds. At that point, interpolation between MM4 levels is conducted to find the pressure at which $bW_a = W$; that pressure is taken to be the location of the cloud base. In the few instances where the retrieved cloud base was lower than the lowest MM4 level, the base was raised to that level and the cloud top was adjusted upward to maintain the condition that $bW_a = W$.

The value of W_a is the theoretical maximum of total liquid water for vertical ascent through the specified layer. Observations of stratiform clouds (Noonkester 1984; Frisch et al. 1995) have shown that actual liquid water totals are sometimes substantially smaller than W_a. For our computations, the cloud liquid water is assumed to be a fraction, b, of the theoretical maximum. We chose a value of $b = 0.03$ to get rough agreement between the retrieved cloud-base altitudes and the few surface observations that were taken under the stratiform cloud. This value is lower than typical values found in the literature (0.1–1.0), but relatively low values should be expected in the circumstances present at 1000 EST, when the clouds were gradually dissipating. Furthermore, it is possible that the clouds were not a single, continuous layer, leading to a value of b that is representative of the overall cloud distribution.

This use of the retrieved W to estimate cloud-base pressure would not be applicable to situations where W is large and the clouds are highly reflective. When the cloud reflectance is greater than about 70%, W cannot be retrieved reliably because small errors in satellite-derived reflectance would give rise to large changes in W (Stephens et al. 1984). For our demonstration case there was no such problem because cloud reflectances were less than 70% in nearly all (96%) of the cloudy pixels. In cases with substantial amounts of highly reflective clouds, a different method of cloud-base retrieval would be needed.

The assumptions used in this cloud-base retrieval method would certainly not be valid in every situation, and there are probably portions of our application domain at 1000 EST where some of the assumptions do not closely represent the cloud conditions. We nevertheless consider the assumptions to be appropriate for this application for two reasons. First, there are no alternatives that appear to offer any substantial advantages. Surface observations are far too sparse to describe the cloud-base altitude variations within the domain. Second, the assumptions are not of primary importance to the ultimate intended effect of the retrievals: to alter selected model fields such that the model produces surface radiation fluxes consistent with the satellite-retrieved cloud characteristics. The achievement of this effect depends not on having highly accurate cloud altitudes, but on causing the model cloud representation to be consistent with the satellite retrievals. The assumptions are acceptable as long as the inclusion of this cloud information in the model does not cause any significant degradation of any aspect of the model's performance. The results for this case, shown later in the paper, indicate no such sign of degradation.

d. Grid-scale cloud fraction

A satellite-derived, three-dimensional, gridded analysis of cloud fraction was generated from the cloud-top and -base retrievals. For each grid box in the MM4 horizontal grid, the satellite pixels located within the grid box were identified and counted (m_{total}). In addition, at each model level, the pixels that were within a cloud layer (having a cloud top higher than the level and a cloud base lower) were counted (m_{cloud}). Then $m_{\text{cloud}}/m_{\text{total}}$ was taken as the cloud fraction (n) at the grid point. This process yielded a three-dimensional analysis of n.

e. Adjustment of relative humidity

The method for adjusting the relative humidity (RH) field begins with the original MM4 cloud fraction equation:

$$n_i = \upsilon_i \text{RH(max)}_i + y_i \qquad (\text{RH(max)}_i \geq \text{RH}_{xi}),$$

$$n_i = 0 \qquad (\text{RH(max)}_i \leq \text{RH}_{xi}), \quad (6)$$

where RH (max)_i is the (nondimensional) maximum RH within the specified layer i, the subscript x refers to a threshold value, and υ and y are empirical coefficients. The layers are defined as low (~970–800 hPa), middle (~800–450 hPa), and high (~450–50 hPa), respectively, with $\upsilon_1 = \upsilon_2 = 4.0$, $\upsilon_3 = 2.5$, $y_1 = y_2 = -3.0$, $y_3 = -1.5$, $\text{RH}_{x1} = \text{RH}_{x2} = 0.75$, and $\text{RH}_{x3} = 0.60$.

At grid points where the satellite-retrieved cloud fraction is nonzero, the relationship in (6) is reversed to solve for the adjusted value of RH, given the retrieved value of n. The distinction between RH and RH (max) is ignored in this solution. For those model grid points where the retrieved value of n is zero, the RH is not

adjusted unless it exceeds RH_x, in which case it is set to RH_x. Below the 970-hPa level, the RH values are not adjusted regardless of the retrieved n, for consistency with the MM4 cloud diagnosis, which extends only to 970 hPa.

The RH adjustments to the gridded model data are made in terms of the model's primary moisture variable, mixing ratio. As a practical matter, the adjustments are applied using the gridpoint nudging facility in MM4 (Stauffer and Seaman 1990), with a nudging coefficient large enough to ensure that the adjustment is complete within a few time steps.

The procedure described above has two important and immediate effects: the humidities may increase in those grid boxes where the satellite retrievals have detected cloud, and the humidities may decrease in those grid boxes where the satellite has detected no cloud. When the model then applies (6) during its subsequent integration, it then may diagnose more cloud cover in some areas than it would have without the adjustment, and less in other areas.

4. Results of humidity adjustment

When the moisture field was adjusted (1000 EST), the adjusted field differed from the original by slightly more than 1%, in terms of nested-grid total water vapor mass. Considering that more than one-third of the grid boxes at this time had some significant cloud fraction, this result implies that the adjustment procedure acted essentially to redistribute the existing water vapor mass, rather than increase or decrease it.

The nature of the adjustments to the humidity fields can be seen in plots of water vapor mixing ratios from MM4 (Fig. 2) at $\sigma = 0.875$ [~1250 m AGL, where $\sigma = (p - p_t)/(p_s - p_t)$ and p_t is the pressure at the top of the model]. This level was chosen because it coincided with the height of a stratiform cloud over western Georgia that had an important effect on the surface solar insolation. Figure 2a is the mixing ratio field at 1000 EST from the MM4; Fig. 2b is this same mixing ratio field after a 5-min integration during which the humidity field (in terms of the mixing ratio) was adjusted to be the same as the 1000 EST analysis derived from the satellite data. Note that the mixing ratio values were increased in western Georgia and in the lee of the Appalachian Mountains in western North Carolina. The assimilated satellite data lowered the mixing ratios in eastern North Carolina and throughout much of Alabama and southern Virginia, where the satellite analysis had found skies to be largely free of clouds. In other areas, the analysis was unchanged. Overall, the adjustment resulted in an increased level of mesoscale detail; however, there were no radiosonde soundings available at 1000 EST to evaluate the accuracy of the analyses.

Initial evaluations of the effects of this humidity field adjustment revealed that the adjustment generated excessive gravity–inertia wave noise in the ensuing forecast. This problem arose from the effect of sudden changes in virtual temperature (T_v), which is a function of the water vapor mixing ratio, on the horizontal geopotential gradient term of the momentum equation. To eliminate this effect, the model temperature field was adjusted simultaneously with the humidity field, such that T_v would remain constant during the adjustments. This is the solution Koch et al. (1997) employed when they encountered the same problem in their experiments. The overall rms temperature change induced by this adjustment was 0.2°C, with the largest value among all the grid points being −1.6°C. This temperature adjustment reduced the gravity–inertia wave activity to levels that occurred in the absence of any humidity assimilation.

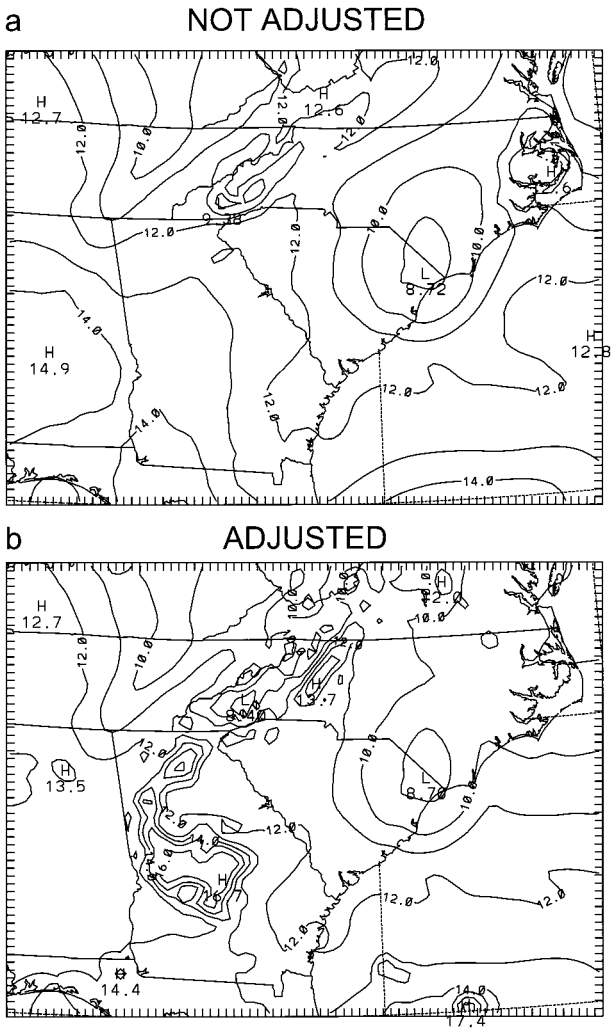

FIG. 2. Water vapor mixing ratios (g kg^{-1}) from the model (a) before (1000 EST) and (b) after (1005 EST) the humidity adjustment. The area shown is the fine-grid model domain, but having excluded the outer four rows and columns.

An alternative method to avoid inducing noise when adjusting the model humidity fields would be to spread

the adjustment throughout the assimilation period (i.e., gradually nudge the humidity values), instead of doing the entire adjustment at the end of the period. This method could involve executing the cloud fraction retrieval procedure with every satellite dataset that was taken during the assimilation period. It would be necessary to revise the model code to temporally interpolate the cloud fraction data and use the fractions to compute humidity adjustments at each time step of the assimilation. This alternative would allow the satellite-derived humidity information to affect the modeled virtual temperatures and, potentially, improve the modeled dynamics. However, the alternative would have provided little benefit for the case described here, considering that the rms temperature adjustments made to hold T_v constant (0.2°C) were considerably smaller than the rms errors in the forecast temperature fields (1.3°C), which are discussed in section 6.

Considering that the primary purpose of the humidity adjustment was to improve the model representation of surface insolation, we examined the insolation fields from the adjusted model (Fig. 3b). Those fields were compared with the fields just before the adjustment, when the model was still relying on assimilated retrievals of τ_{eff} to control the insolation computations (Fig. 3a). The goal of the adjustment had been been to achieve a match between these fields. The overall patterns and magnitudes of the two fields are generally similar. The adjustment succeeded in getting the modeled cloud-induced insolation reductions to be distributed according to the satellite-observed cloud cover. Still, there are significant differences between the fields with regard to the horizontal extent of the areas with low insolation values (i.e., $\leq$400 W m^{-2}) and the magnitudes at the places with local minima. The insolation values from the adjusted model are excessively uniform within cloudy areas, with sharp boundaries between the cloudy and clear areas.

The character of the insolation fields from the adjusted model can be better understood by considering the distribution of retrieved cloud fractions, which had been used to specify the humidity adjustments. Figure 4 depicts a vertical section of retrieved cloud fractions along the line marked in Fig. 3b. In the western part of the section, there was a layer about 100 hPa thick with cloud fractions >80%, whereas in the eastern part, the layer with high cloud fractions was very thin. From these data, the model was adjusted to have a thicker zone of high relative humidity in the western part than in the eastern part. Despite this east–west contrast in humid-layer thickness, the adjusted model had nearly constant values of insolation along the entire line. The reason for the discrepancy is that the MM4 cloud radiation parameterization confines clouds to three discrete layers: low, middle, and high. The model-diagnosed cloud cover for each predefined layer depends on the *maximum* relative humidity among the σ levels within the layer, and does not recognize differences in the

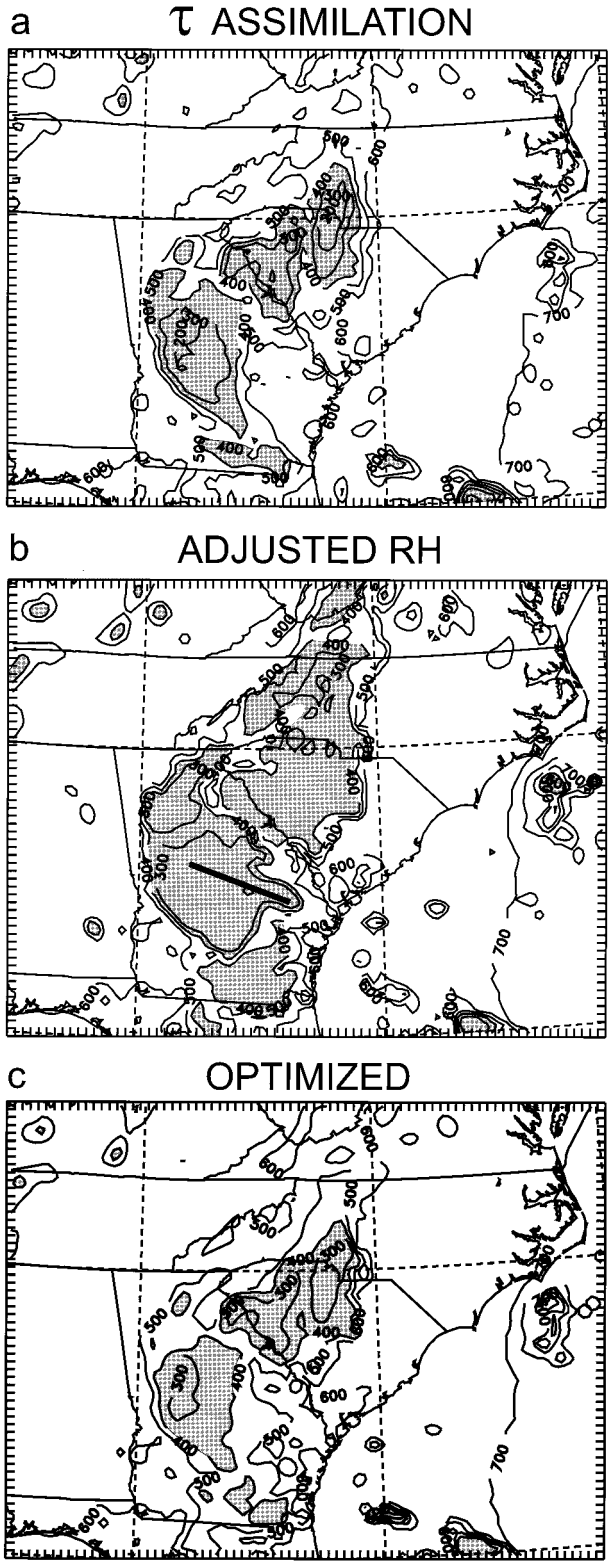

FIG. 3. Surface insolation (W m^{-2}) at 1005 EST from (a) the model with assimilation of satellite-retrieved τ_{eff} data, (b) the model with adjusted RH, and (c) the model with adjusted RH and the optimized cloud transmittance formulation. Areas with values <400 W m^{-2} are shaded gray. The thick solid line in (b) indicates the location of the cross section in Fig. 4.

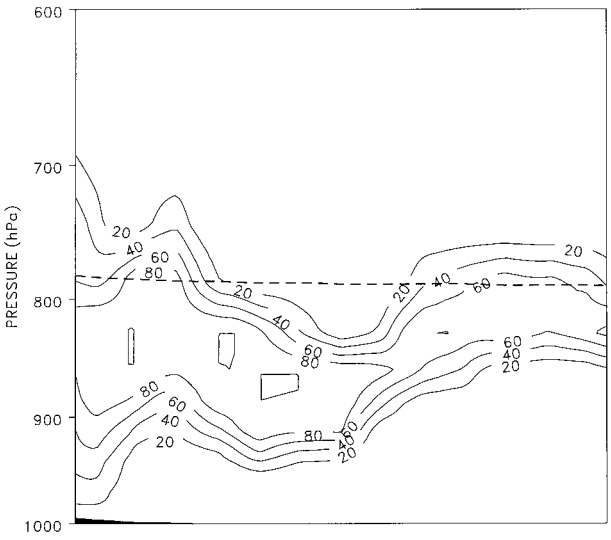

FIG. 4. A cross section of the cloud fraction (%), as retrieved from 1000 EST satellite data. The dashed line is the border (σ surface) between zones identified with low and middle clouds in the model. The cross section goes from northwest (left) to southeast (right) along the line marked in Fig. 3b.

depth of the high humidity zone within the layer. This problem was recognized to occur also in the Eta Model at the National Centers for Environmental Prediction (Rogers et al. 1996). We chose to address this problem in the MM4 cloud diagnosis method by altering the radiation parameterization method, as discussed in the next section.

5. Solar radiation modeling

a. Reformulation of parameterization

The standard MM4 computes the solar transmittance of a cloudy atmosphere as a function of effective transmittance factors for cloud absorption (τ_{ac}) and scattering (τ_{sc}) at the scale of the model grid. Those factors are defined as

$$\tau_{ac} = \prod_{i=1}^{3} [1 - (1 - \tau_{ai})n_i] \quad \text{and}$$

$$\tau_{sc} = \prod_{i=1}^{3} [1 - (1 - \tau_{si})n_i], \tag{7}$$

where τ_{ai} and τ_{si} are tabulated coefficients and n_i, as before, is the cloud fraction for one of the three layers of clouds represented by the MM4 (Benjamin 1983).

Despite the shortcomings of the MM4 parameterization (such as the use of separate effective transmittances for absorption and scattering), we chose not to replace the entire parameterization with another method for our experiments, but to alter the existing method to a minimal degree. Every parameterization is an approximation of the true physics, with room for tuning and improvement. As with the standard formulations, our revised MM4 formulations are products of transmittance coefficients for three layers, but with each layer subdivided according to σ layers and with a tuning parameter inserted. Specifically, the formulations for τ_{ac} and τ_{sc} were changed to

$$\tau_{ac} = \prod_{i=1}^{3} \left\{ \prod_{k=1}^{K_i} [1 - (1 - \tau_{ai}^{C_i\zeta_{ik}})n_{ik}] \right\} \quad \text{and}$$

$$\tau_{sc} = \prod_{i=1}^{3} \left\{ \prod_{k=1}^{K_i} [1 - (1 - \tau_{si}^{C_i\zeta_{ik}})n_{ik}] \right\}, \tag{8}$$

where K_i is the number of σ levels within layer i,

$$n_{ik} = \upsilon_i \mathrm{RH}_{ik} + y_i \qquad (\mathrm{RH} \geq \mathrm{RH}_{xi}),$$

$$n_{ik} = 0 \qquad (\mathrm{RH} \leq \mathrm{RH}_{xi}),$$

RH_{ik} is the relative humidity at level ik, C_i is an empirically determined constant for each layer,

$$\zeta_{ik} = \frac{\Delta z_{ik}}{\sum_{k=1}^{K_i} \Delta z_{ik}},$$

and Δz_{ik} is the depth of σ layer ik. The variable ζ_{ik} represents the depth of a σ layer in terms of a fraction of the predefined layer i.

The relationship between the original and altered formulations can be elucidated by considering the case where $n_{ik} = n_i = 1$. In that case, the original formulation for τ_{sc} (7) becomes

$$\tau_{sc} = \prod_{i=1}^{3} \tau_{si}. \tag{9}$$

The altered formulation becomes

$$\tau_{sc} = \prod_{i=1}^{3} \left\{ \prod_{k=1}^{K_i} \tau_{si}^{C_i\zeta_{ik}} \right\} = \prod_{i=1}^{3} \{\tau_{si}^{r_i}\}, \tag{10}$$

where

$$r_i = \sum_{k=1}^{K_i} C_i\zeta_{ik} = C_i \sum_{k=1}^{K_i} \zeta_{ik} = C_i. \tag{11}$$

So, the two formulations produce the same result if $C_i = 1$. The actual values of C_i used in our experiments were determined by the optimization procedure described below.

b. Optimization

1) STRATEGY

The values of the empirical coefficients, C_i, were computed by considering their ultimate effect on the model computations of surface insolation under cloudy conditions, $Q^M_{s\,(\mathrm{cloudy})}$. The values of C_i affect $Q^M_{s\,(\mathrm{cloudy})}$ by way of (8) and through a series of equations for computing $Q^M_{s\,(\mathrm{cloudy})}$ from τ_{ac} and τ_{sc} (Benjamin 1983), which

TABLE 2. Number of model grid points with clouds in each layer combination.

Low	Mid	High	Count
			2752
•			413
	•		557
•	•		641
		•	12
•		•	1
	•	•	9
•	•	•	23

contain several additional terms. Values of C_i were computed so as to minimize differences between $Q^M_{s\,(\text{cloudy})}$ and $Q^S_{s\,(\text{cloudy})}$, where $Q^S_{s\,(\text{cloudy})}$ were the insolation values that resulted from assimilating τ_{eff} retrieved from visible satellite data. Those differences were represented by objective functions J_i, defined as

$$J_i = \sum_{j=1}^{N_i} [Q^M_{s\,(\text{cloudy})j}(C_i) - Q^S_{s\,(\text{cloudy})j}]^2, \qquad (12)$$

where N_i is the number of MM4 grid points with cloud in layer i only. The values of C_i that minimize J_i were computed using the iterative quasi-Newton gradient method. In this process, the variables that factor into $Q^M_{s\,(\text{cloudy})j}$ that depend on the model state were computed using 1005 EST model data, in which the humidity had been adjusted as described above. The values of $Q^S_{s\,(\text{cloudy})j}$ were from the model run that assimilated τ_{eff}, extended 5 min to 1005 EST to provide a perfect time match with the data in $Q^M_{s\,(\text{cloudy})j}$.

One way to solve for C_i would be to minimize an objective function for all cloudy grid points simultaneously, considering that typically there are grid points with clouds in more than one layer. However, the problem was simplified by solving for C_1 while operating (12) on the subset of grid points that had only low cloud. This simplification was possible because there were many such points. The numbers of grid points with each possible combination of cloud layering are given in Table 2. Likewise, C_2 was found using grid points with middle cloud only. The optimization results were $C_1 = 1.02$ and $C_2 = 3.95$. Because there were few points with high cloud, no optimization was done for that layer and we set $C_3 = 1$.

Considering that there were many grid points with low and middle clouds combined, an additional optimization was done with those points. For this optimization, the value of C_2 was held constant at 3.95 while C_1 was optimized, because C_2 was based on more grid points than was C_1. An objective function was minimized by adjusting C_1 while including points with either low and middle cloud combined or low cloud alone. The resulting value of C_1 was close to the value computed with only low clouds (a 13% difference). In the forecast experiments, $C_1 = 1.02$ was used.

2) EFFECTIVENESS

The effectiveness of the optimization was evaluated with scatterplots of surface insolation values, in which $Q^M_{s\,(\text{cloudy})}$ was plotted against $Q^S_{s\,(\text{cloudy})}$ at 1005 EST. The four plots (Fig. 5) correspond to four choices of the method to compute $Q^M_{s\,(\text{cloudy})}$: (a) the original ''standard'' MM4 data and formulation; (b) the model with RH adjusted according to satellite data and the standard MM4 cloud transmittance formulation; (c) the model with RH adjusted and the cloud transmittances given as per (8), with $C_1 = C_2 = C_3 = 1$; and (d) the model with RH adjusted and the cloud transmittances from (8), with the optimized values of C_i.

With the standard model data and formulation, there was essentially no correlation between $Q^M_{s\,(\text{cloudy})}$ and $Q^S_{s\,(\text{cloudy})}$ (Fig. 5a). Most of the points lie below the diagonal, indicating that the standard model data and formulation resulted in a negative insolation bias. The adjustment of RH reduced the scatter (Fig. 5b), with the clear grid points falling on the diagonal (at the upper right) due to their complete agreement between $Q^M_{s\,(\text{cloudy})}$ and $Q^S_{s\,(\text{cloudy})}$. The change of cloud transmittance formulation altered the distribution of the cloudy points (Fig. 5c vs Fig. 5b), but substantial scatter remained. The optimization of the C_i (Fig. 5d) reduced the scatter and the bias. These plots make it clear that the latter configuration provided the best agreement with the satellite-derived insolation.

Some sample statistics were calculated from the $Q^M_{s\,(\text{cloudy})} - Q^S_{s\,(\text{cloudy})}$ differences for the situations plotted in Figs. 5c and 5d (Table 3). The optimization process reduced the bias by a factor of 8 and the standard deviation by a factor of 2.

A horizontal plot of the insolation from the model with adjusted RH and optimized C_i is in Fig. 3c. Note that there is very good agreement between this plot and the one with model assimilation of τ_{eff} (Fig. 3a) in terms of the position, shape, and extent of the areas with cloud-induced depressions of insolation. There remains some disagreement in the magnitude of the depressions in some areas, such as in western Georgia.

Overall, the adjustment of RH and the optimization of the cloud transmittance parameterization largely succeeded in making the model-computed insolation agree with the insolation derived with the aid of satellite retrievals of τ_{eff}. The question then was, to what extent would the forecasts from the adjusted, optimized model represent an improvement from forecasts made with the standard model? We present results of these forecasts in the next section.

6. Forecast experiments

The initial data for the experimental forecasts were from the 1000 EST analysis that was created by assimilating cloud radiative parameters over the 0700–1000 EST period. Two forecasts were run from 1000 to 1900

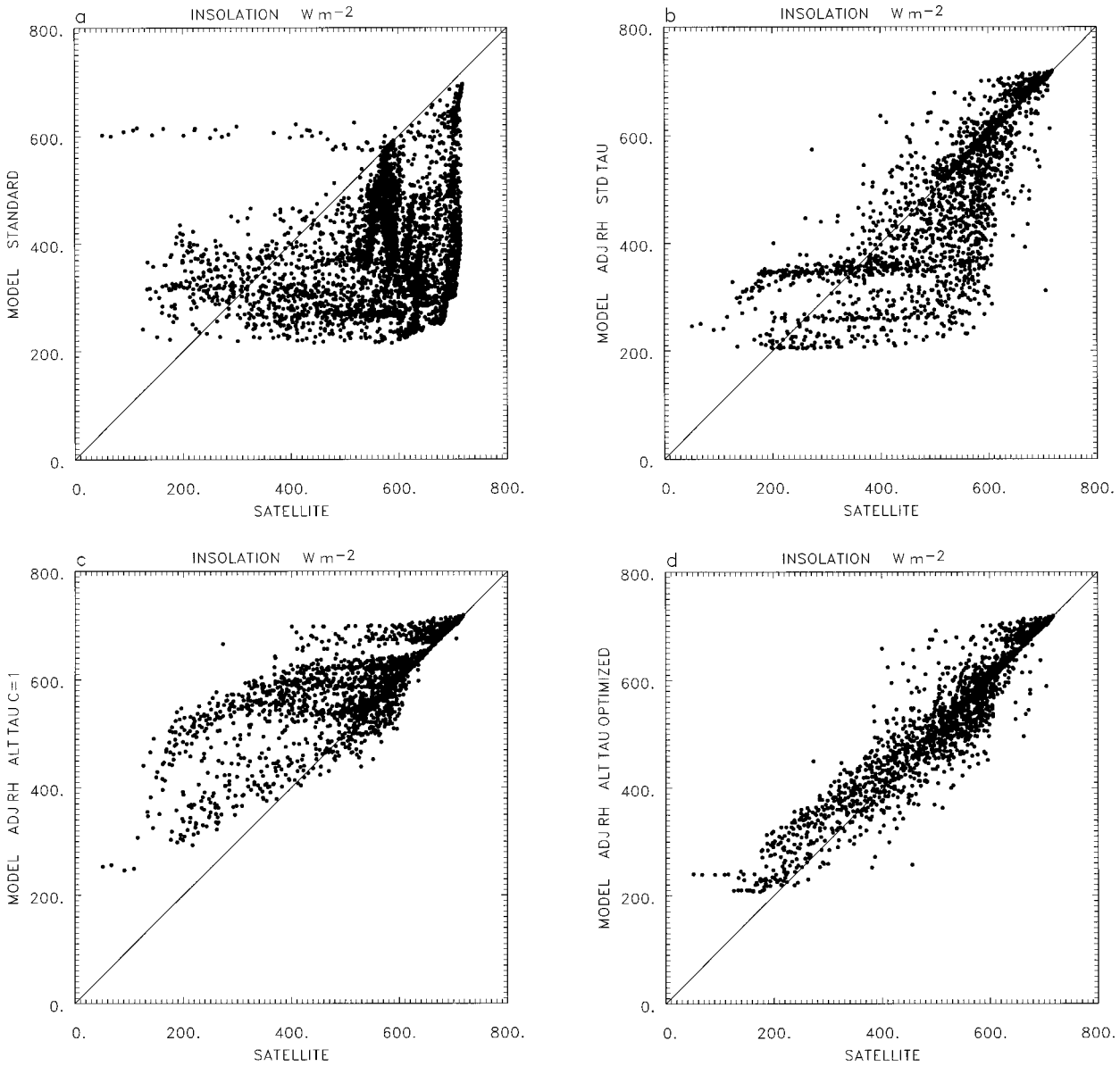

FIG. 5. Scatterplots of the surface insolation (W m^{-2}) at each grid point in the analysis domain at 1005 EST. On every frame, the horizontal axis is the value from the model with assimilation of τ_{eff} from satellite retrievals. The vertical axes are the insolation values from (a) the standard MM4 data and formulation, (b) the model with adjusted RH, (c) the model with adjusted RH and the altered cloud transmittance formulation, and (d) the model with adjusted RH and the optimized cloud transmittance formulation. The diagonal is marked on each frame.

EST. One was made with the standard MM4 formulation and the other was made with adjusted RH (over the period 1000–1005 EST, as described above) and the reformulated, optimized solar radiation parameterization. These experiments will be referred to, respectively, as the standard and adjusted forecast experiments.

TABLE 3. Statistics of differences between $Q^M_{s\,(\text{cloudy})}$ and $Q^S_{s\,(\text{cloudy})}$.

	Mean (W m^{-2})	Std dev (W m^{-2})
RH adjusted, $C_i = 1$	85	96
RH adjusted, optimized C_i	10	51

An initial evaluation of the forecasts was made at the 1300 EST point. At that time, the forecasts of surface insolation were compared with a reference insolation field. The reference consisted of the 1300 EST insolation values from an assimilation experiment in which satellite-retrieved cloud radiative parameters were assimilated throughout the 0700–1300 EST period. This field was a reference in the sense that a forecast result that matches this field is the best one could hope to obtain from the adjusted model.

The areas of low insolation in the reference field at 1300 EST (Fig. 6a) were more patchy than at 1000 EST (Fig. 3a), due to the intervening partial dissipation of the stratiform clouds and the development of convective clouds. The insolation field from the standard forecast (Fig. 6b) was vastly different from the reference field, with low values over most of the domain. The adjusted forecast produced an insolation field (Fig. 6c) that roughly matched the reference field, although the degree of smoothness is quite different. The reference and adjusted forecast fields both had relatively low values extending from north-central South Carolina to western Georgia and along the Appalachian Mountains from northern Georgia to western Virginia. Some areas of low insolation in the reference field were associated with convective cloud fields that were not represented in the adjusted model forecast. Examples of these areas are in southeastern Georgia and central Tennessee.

The differences in insolation between the forecasts gave rise to apparent differences in surface heating. Those heating differences were evaluated by considering the 1300 EST shelter-height (2 m) temperatures, which were diagnosed from the model output and compared with surface observations. There were 103 observations available for comparison within the domain. For the standard model forecast, the bias was −0.9°C, the error standard deviation was 1.6°C, and the correlation coefficient was 0.75. The negative bias was consistent with the excessive diagnosed cloud cover, represented as low insolation values in Fig. 6b. For the adjusted model forecast, the bias (0.5°C) had a smaller magnitude and the error standard deviation (1.5°C) and correlation coefficient (0.76) were about the same as in the standard model forecast. This impact of the adjustment on the shelter-height temperatures was smaller than the impact on insolation (Figs. 6b,c), which is logical considering the time lags involved in energy exchange between the surface, the soil, and the overlaying air. The adjusted forecast errors represent only a slight degradation from the errors in the reference analysis (in which satellite-retrieved cloud parameters were assimilated through 1300 EST), where the bias was 0.4°C and the standard deviation was 1.4°C. Thus, with regard to shelter-height temperatures, the forecast had nearly the same accuracy as an analysis that had the benefit of input from three more hourly satellite datasets.

The fidelity of the adjusted forecast, with respect to the reference analysis at 1300 EST, was apparent also in the wind fields and boundary layer development (Fig. 7b). The adjusted forecast had the same primary features of moisture divergence, wind vectors, and boundary layer depth as in the reference analysis (not shown). Moisture divergence was present at low levels in the stratiform cloud area, with moisture convergence on each side of that area. A weak updraft was present in the eastern part of the domain in association with the sea breeze and a stronger updraft occurred over the high ground to the northwest of the stratiform cloud area.

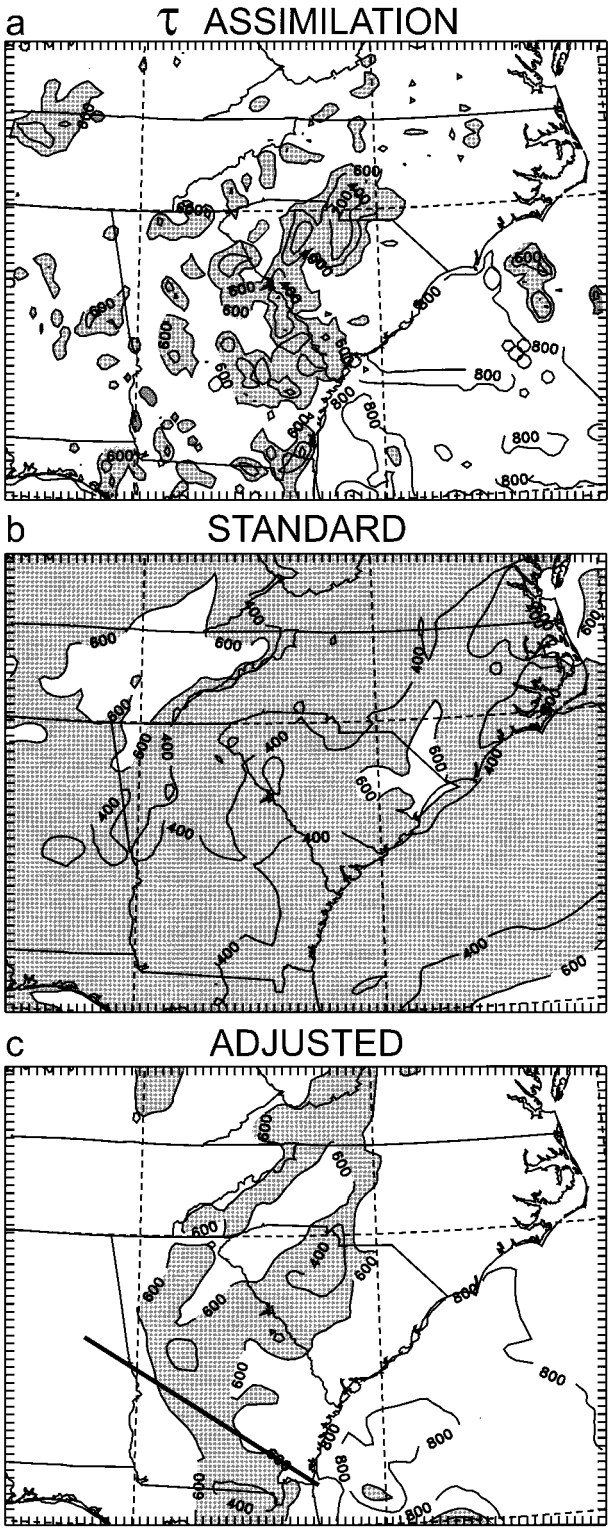

FIG. 6. Surface insolation (W m^{-2}) at 1300 EST from (a) the reference field, as defined in the text; (b) the forecast with the standard model; and (c) the adjusted forecast. Areas with values $<$600 W m^{-2} are shaded gray. The thick solid line in (c) indicates the location of the cross section in Fig. 7.

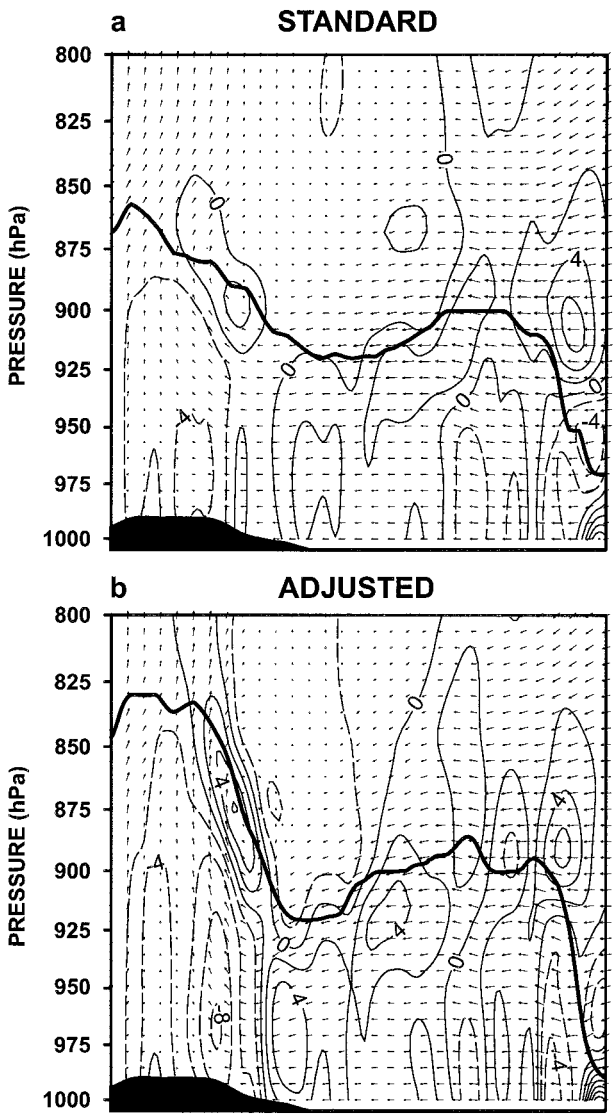

FIG. 7. Cross sections of wind and moisture divergence at 1300 EST from the (a) standard and (b) adjusted forecasts. The cross sections go from northwest (left) to southeast (right) along the line shown in Fig. 6c. The contour interval is 2×10^{-7} s^{-1}, with negative contours dashed. The vector scaling is 6 m s^{-1} and 0.6 Pa s^{-1} per vector interval in the horizontal and vertical directions, respectively. The heavy solid line marks the top of the boundary layer, as diagnosed by the MM4.

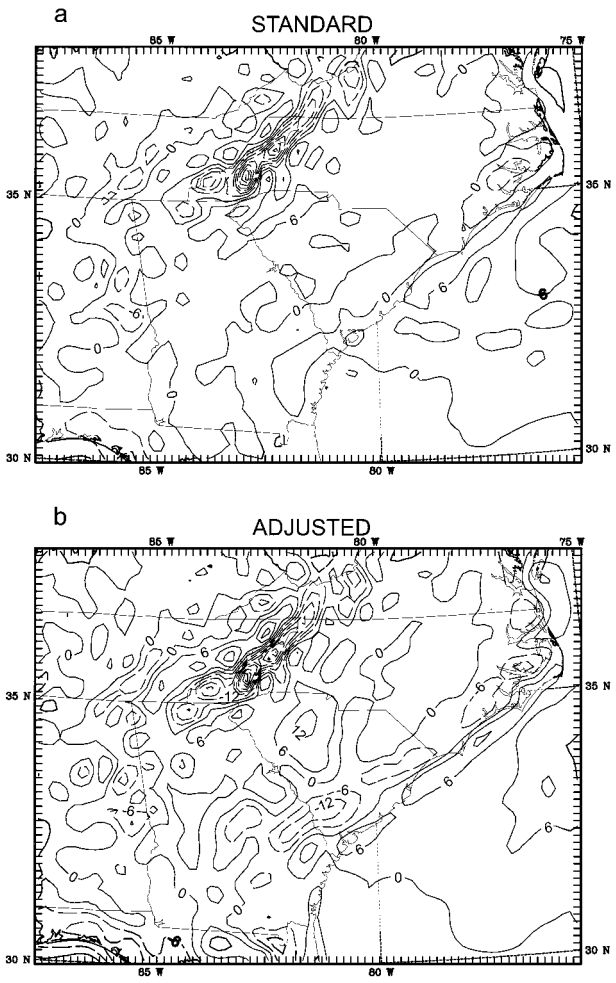

FIG. 8. Moisture divergence at 1600 EST at $\sigma = 0.985$ (about 150 m above ground) from the (a) standard and (b) adjusted model forecasts. Contours are at intervals of 6×10^{-7} s^{-1}.

Corresponding with these circulation features, boundary layer development was suppressed over the stratiform cloud area, with deeper development on each side of the area. This pattern of boundary layer development is consistent with the pattern of convective cloud development that was observed (Fig. 1b). In contrast, the mesoscale features were largely washed out in the standard forecast (Fig. 7a).

The adjusted and standard forecasts continued to be significantly distinct from each other well beyond 1300 EST. At 1600 EST, the adjusted forecast moisture divergence field (Fig. 8b) had a band of divergence running from central North Carolina through western Georgia, in the area where stratiform clouds had been present. Moisture convergence was forecast just inland from the coast and along the Appalachian crest, the northern parts of which had relatively little convective available potential energy. Other areas of forecast moisture convergence were in eastern Alabama and south-central Georgia, on opposite sides of the band of divergence. Those areas correspond roughly to areas where vigorous convective development occurred later. The standard forecast of moisture divergence (Fig. 8a) had much less convergence than the adjusted forecast along the coast, and lacked the pronounced features that the adjusted forecast had in central Georgia.

The experimental forecasts valid at 1900 EST provide an opportunity to directly consider the effect of the humidity adjustment on the accuracy of the model water vapor field. From the time the adjustment was made (1000 EST), there were no verification data available until 1900 EST (0000 UTC 24 Aug 1993), when ra-

diosonde data were taken at eight stations within the domain. Profiles of model data were interpolated to the radiosonde sites and differences were computed at 25-hPa intervals from 400 to 1000 hPa. Dewpoint temperature was used as the differencing parameter because, unlike mixing ratio, it does not systematically vary by orders of magnitude over the layer being considered. The rms differences for the adjusted forecast were less than or equal to the differences for the standard forecast at all pressure levels. When averaged over all pressure levels, the rms differences for the standard and adjusted forecasts were 5.8° and 5.1°C, respectively, and the correlation coefficients were 0.81 and 0.84, respectively. Considering that model temperatures were adjusted along with water vapor concentrations (to hold T_v constant), difference statistics for temperatures were computed also. The differences were generally small and similar for the two forecasts, with vertically averaged rms values of 1.2° and 1.3°C, respectively, and correlation coefficients of 0.68 and 0.66, respectively, for the standard and adjusted forecasts. The number of profiles available to compute these statistics was small, but the statistics suggest that the humidity adjustments had no detrimental effect on the modeled humidity or temperature fields, and may have even improved the humidity field.

7. Conclusions

The methods we developed for adjusting model data and parameters using satellite data were shown, by our experimental results, to be highly effective at enabling the model to retain the information provided by the satellite and apply that information throughout a forecast. The primary satellite information was an analysis of stratiform cloudiness and a quantitative estimate of the clouds' effect on the surface insolation. The adjusted model, in forecast mode, produced a surface insolation field that closely agreed with an analysis derived from satellite retrievals. The agreement, in both cloudy and clear areas, was far greater than was present without the adjustment.

Our forecast experiments indicated that the model adjustments had a pronounced impact on some aspects of the forecast for at least 6 h and that the impacts were generally beneficial. The forecast with the adjusted model was more accurate than a standard forecast made without the adjustment, as measured by agreement with surface observations of shelter-height temperatures. The adjustment also appeared to be beneficial with regard to forecasting the potential for development of deep convective clouds, considering forecasts of boundary layer development and moisture convergence.

While the data available for quantitative evaluation of our results were few, the results suggest that there is promise for application of our adjustment methods to other situations where shading of the ground by stratiform clouds is an important factor in the short-term weather forecast. We do not know whether it would be necessary to perform a tuning (optimization) of the model radiation parameterization for every application, or whether the empirical coefficients found optimal for our application would produce acceptable results in general. It is certainly possible to perform a separate optimization for each case, but if the coefficients vary substantially from one case to another it would be an indication that the parameterization method in the model should be improved or replaced.

Acknowledgments. We thank T. Stoffel of the National Renewable Energy Laboratory for providing the pyranometer data used for calibrating the visible satellite data. We also thank R. P. d'Entremont, W. J. Lipton, D. C. Norquist, and two anonymous reviewers for suggesting improvements to the manuscript and A. Hobgood and T. Walker for assistance in preparing figures. Surface weather observation data were provided by the USAF Combat Climatology Center. This research was supported by the Air Force Office of Scientific Research under Project 2310 and by the Department of Defense High Performance Computing Shared Resource Center, Army Corps of Engineers Waterways Experiment Station.

REFERENCES

Albers, S. C., J. A. McGinley, D. L. Birkenheuer, and J. R. Smart, 1996: The Local Analysis and Prediction System (LAPS): Analysis of clouds, precipitation, and temperature. *Wea. Forecasting,* **11,** 273–287.

Anthes, R. A., 1977: A cumulus parameterization scheme utilizing a one-dimensional cloud model. *Mon. Wea. Rev.,* **105,** 270–286.

Benjamin, S. G., 1983: Some effects of surface heating and topography on the regional severe storm environment. Ph.D. dissertation, The Pennsylvania State University, 265 pp. [Available from University Microforms International, 300 N. Zeeb Rd., Ann Arbor, MI 48106-1346.]

——, and N. L. Seaman, 1985: A simple scheme for objective analysis in curved flow. *Mon. Wea. Rev.,* **113,** 1184–1198.

Errico, R. M., and G. T. Bates, 1988: Implicit normal-mode initialization of the PSU/NCAR mesoscale model. NCAR Tech. Note NCAR T/N-312+IA, 112 pp. [Available from NCAR Information Services, P.O. Box 3000, Boulder, CO 80307.]

Frisch, A. S., C. W. Fairall, and J. B. Snider, 1995: Measurement of stratus cloud and drizzle parameters in ASTEX with a K_α-band Doppler radar and a microwave radiometer. *J. Atmos. Sci.,* **52,** 2788–2799.

Koch, S. E., A. Aksakal, and J. T. McQueen, 1997: The influence of mesoscale humidity and evapotranspiration fields on a model forecast of a cold-frontal squall line. *Mon. Wea. Rev.,* **125,** 384–409.

Lipton, A. E., 1993: Cloud shading retrieval and assimilation in a satellite–model coupled mesoscale analysis system. *Mon. Wea. Rev.,* **121,** 3062–3081.

Macpherson, B., B. J. Wright, W. H. Hand, and A. J. Maycock, 1996: The impact of MOPS moisture data in the U.K. Meteorological Office mesoscale data assimilation scheme. *Mon. Wea. Rev.,* **124,** 1746–1766.

Noonkester, V. R., 1984: Droplet spectra observed in marine stratus cloud layers. *J. Atmos. Sci.,* **41,** 829–845.

Rogers, E., T. L. Black, D. G. Deaven, G. J. DiMego, Q. Zhao, M. Baldwin, N. W. Junker, and Y. Lin, 1996: Changes to the op-

erational ''early'' Eta analysis/forecast system at the National Centers for Environmental Prediction. *Wea. Forecasting,* **11,** 391–413.

Smith, W. L., 1983: The retrieval of atmospheric profiles from VAS geostationary radiance observations. *J. Atmos. Sci.,* **40,** 2025–2035.

Stauffer, D. R., and N. L. Seaman, 1990: Use of four-dimensional data assimilation in a limited-area mesoscale model. Part I: Experiments with synoptic-scale data. *Mon. Wea. Rev.,* **118,** 1250–1277.

Stephens, G. L., S. Ackerman, and E. A. Smith, 1984: A shortwave parameterization revised to improve cloud absorption. *J. Atmos. Sci.,* **41,** 687–690.

Vukicevic, T., and J. Paegle, 1989: The influence of one-way interacting lateral boundary conditions upon predictability in bounded numerical models. *Mon. Wea. Rev.,* **117,** 340–350.

Wolcott, S. W., and T. T. Warner, 1981: A moisture analysis procedure utilizing surface and satellite data. *Mon. Wea. Rev.,* **109,** 1989–1998.

Wu, X., and W. L. Smith, 1992: Assimilation of ERBE data with a nonlinear programming technique to improve cloud-cover diagnosis. *Mon. Wea. Rev.,* **120,** 2009–2024.

Zhang, D.-L., and R. A. Anthes, 1982: A high-resolution model of the planetary boundary layer—Sensitivity tests and comparison with SESAME-79 data. *J. Appl. Meteor.,* **21,** 1594–1609.